Electronic supplementary information for

Stabilizing the active phase of iron-based Fischer-Tropsch catalysts for lower olefins: mechanism and strategy

Ou Zhuo,[a] Lijun Yang,[*a] Fujie Gao,[a] Bolian Xu,[a] Qiang Wu,[a] Yining Fan,[a] Yu Zhang,[b] Yufei Jiang,[a] Runsheng Huang,[b] Xizhang Wang,[*a] and Zheng Hu[*a]

[a]Key Laboratory of Mesoscopic Chemistry of MOE, School of Chemistry and Chemical Engineering, Nanjing University, Nanjing 210023, China
[b]School of Physics, Nanjing University, Nanjing 210093, China
[*]Correspondence: lijunyang@nju.edu.cn, wangxzh@nju.edu.cn, zhenghu@nju.edu.cn

Table of Contents

Experimental Procedures

Preparation of hNCNC and hCNC. The supports were prepared at 800 °C by the in situ MgO template method as detailed in our recent paper.[1] hNCNC-1, hNCNC-2 and hNCNC-3 were obtained with different precursors of benzene/pyridine mixture (v/v 3:1), pyridine, and 3-aminopyridine-saturated pyridine solution, leading to a tunable N content of 3.0, 8.1, and 12.0 at.%, respectively. Benzene was used as the precursor for the preparation of hCNC. The Brunauer-Emmett-Teller (BET) specific surface areas (S_{BET}) and element contents of the samples are listed in Table S1.

Characterization. The sizes, morphologies, structures and compositions of the samples were characterized by transmission electron microscopy (TEM, JEOL JEM-2100F equipped with an energy-dispersive spectrometer operating at 200 kV), scanning electron microscope (SEM, Hitachi S4800 at 10 kV), X-ray diffraction (XRD, Bruker D8 Advance A25, Co $K_{\alpha 1}$ radiation of 1.78897 Å with Fe filter of 0.02 mm thickness), and X-ray photoelectron spectroscopy (XPS, ULVAC-PHI INC, PHI 5000 VersaProbe), respectively. The thermogravimetry (TG, Netzsch STA449F3) analysis was carried out in 20 vol % O_2-containing Ar of 20 sccm at a rate of 10.0 °C min^{-1}.

N_2 adsorption/desorption isotherm was measured on Thermo Fisher Scientific Surfer Gas Adsorption Porosimeter at 77 K after degassed at 300 °C for 6 hours. S_{BET} was calculated using the BET method based on the adsorption data in linear relative pressure (p/p_0) range of 0.05-0.30. From the adsorption branch of N_2 isotherm, micropore size distributions and micropore volumes were calculated by using Horvath-Kawazoe method (N_2 on graphite), and meso- and macro-pore size distributions were calculated by using Barrett-Joyner-Halenda method. Mesopore surface area was obtained from t-plot analysis (calculation standard: de Boer).

^{57}Fe Mössbauer spectra were collected at room temperature with a Wissel Mössbauer spectrometer. The spectrometer was calibrated using an α-Fe foil. To avoid oxidation of Fe_xC_y nanoparticles, the reactor with the spent catalyst was cooled down in Ar, sealed, and then transferred into an Ar-filled glovebox. Finally, the spent catalyst was sealed in a home-made sample box for the Mössbauer measurement.

Details of theoretical calculations. All spin-unrestricted density functional theory (DFT) calculations were carried out using the DMol^3 Package embedded in Materials Studio 8.0.[2-3] The generalized gradient-corrected Perdew-Burke-Ernzerhof (PBE/GGA) functional,[4] along with a double numerical basis set including p-polarization function (DNP), is applied for all calculations.[5-7] Dispersion-corrected DFT (DFT-D) scheme is used to describe the van der Waals (vdW) interaction. The coordinates were relaxed with Broyden-Fletcher-Goldfarb-Shanno (BFGS) optimization method.[8] The tolerances of energy and force were 1×10^{-5} Ha and 0.002 Ha/Å, respectively. The Monkhorst-Pack k-point mesh was sampled with a separation of about 0.023 Å^{-1} in the Brillouin zone. The free energies of the reactions at the temperature of 350 °C were calculated with the partial hessian vibrational analysis (PHVA) method.[9]
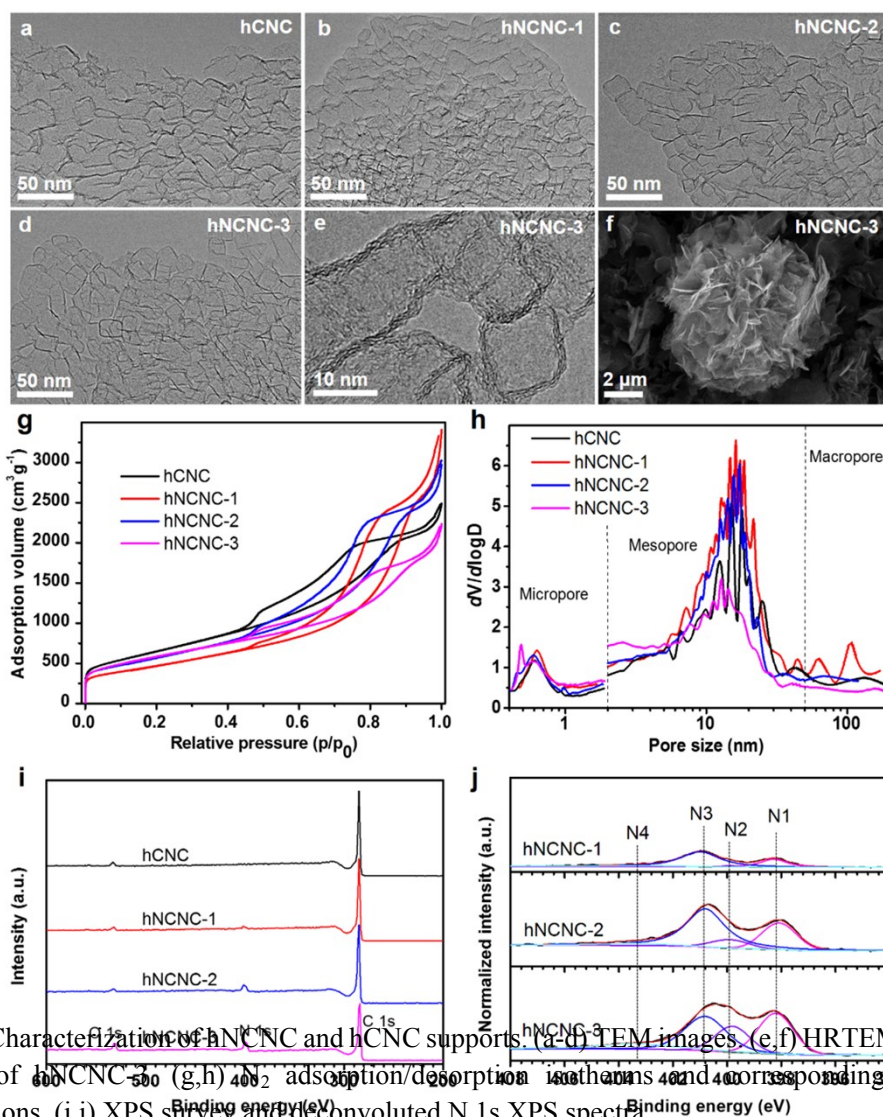
Fig. S1 Characterization of hNCNC and hCNC supports. (a-d) TEM images. (e,f) HRTEM and SEM images of hNCNC-3. (g,h) N_2 adsorption/desorption isotherms and corresponding pore size distributions. (i,j) XPS survey and deconvoluted N 1s XPS spectra.

Note: N 1s peak intensities were normalized by C 1s peak intensity. N1s XPS spectra were deconvoluted into pyridinic (398.2±0.1 eV), pyrrolic (399.9±0.1 eV), graphitic (400.9±0.1 eV), and pyridine-N-oxided (403.4±0.1 eV) species, denote as N1, N2, N3 and N4, respectively[1].

All samples present a 3D hierarchical architecture constructed by interconnected hollow nanocages of 10-30 nm in size and 3~7 graphitic layers in shell thickness (a-f), which provide us a series samples with the close high S_{BET} and similar pore size distributions but tunable N contents (g-j, see Table S1).
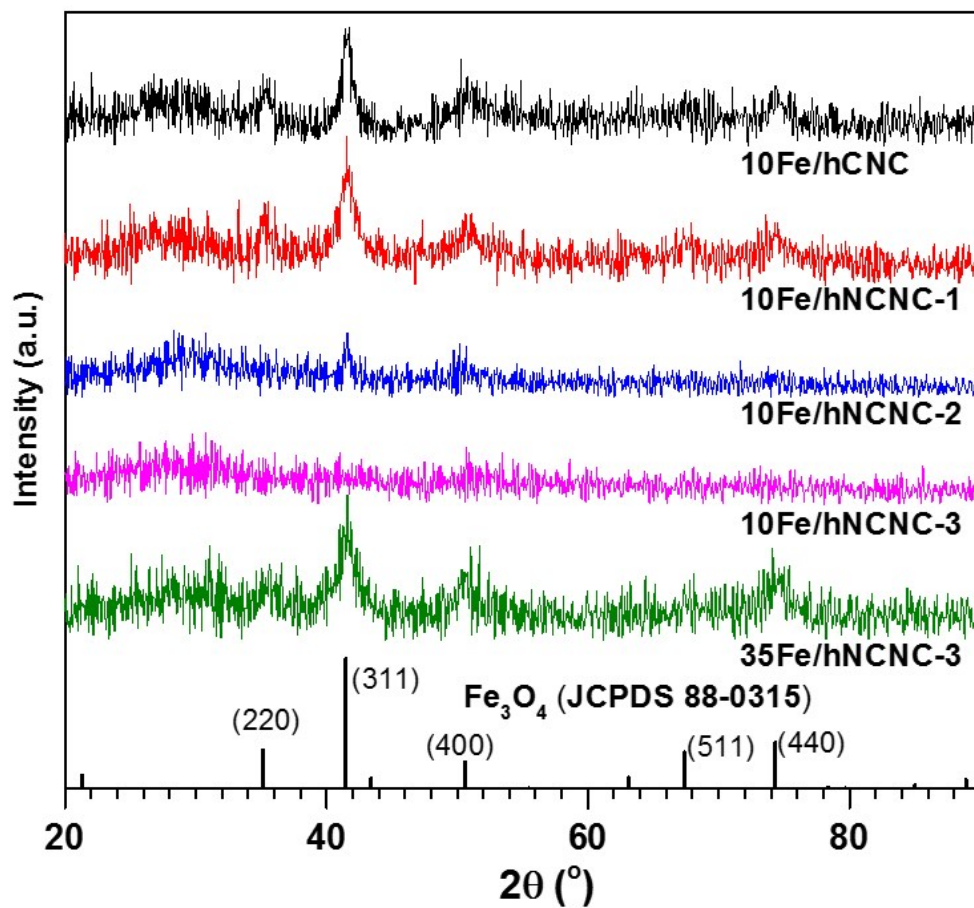
Fig. S2 XRD patterns of a series of fresh catalysts.

The diffraction peaks at 2θ values of 35.2, 41.5, 50.6, 67.4 and 74.3° are assigned to Fe_3O_4.
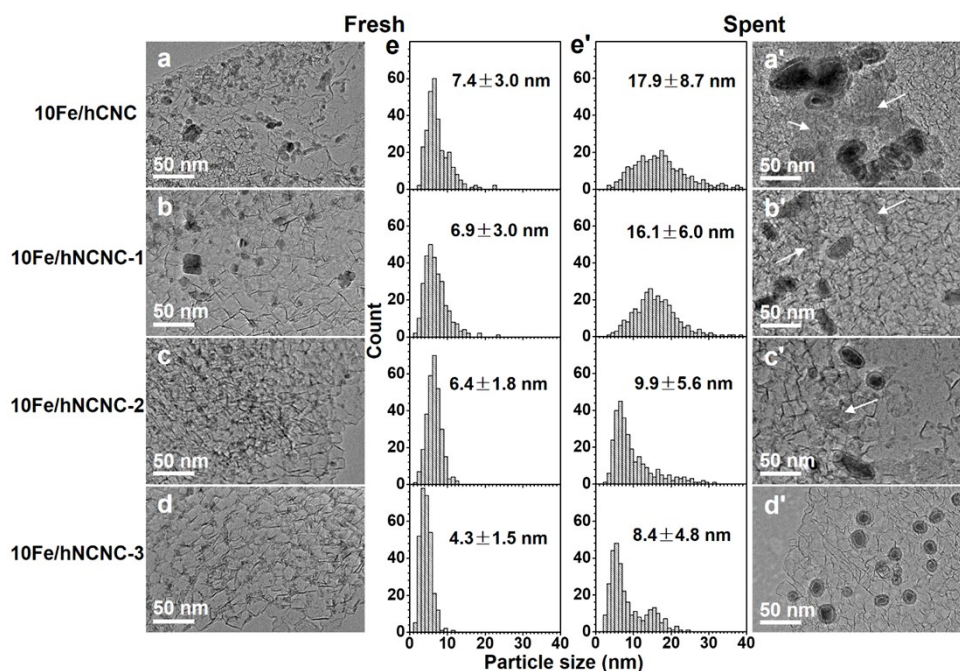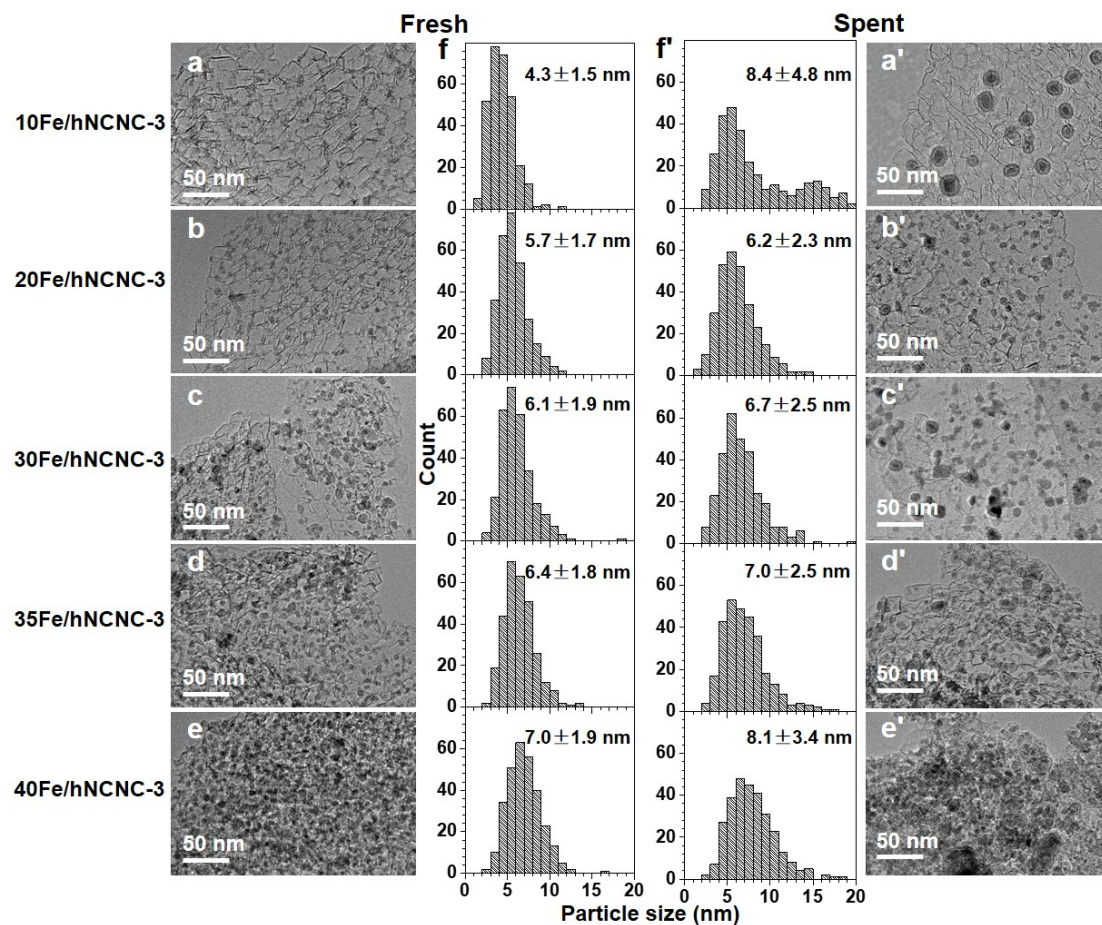
Fig. S3 TEM images (a-d, a'-d') and particle size distributions (e, e') of fresh catalysts (left) and spent catalysts after 60 h on stream in FTO (right). The catalysts have the similar Fe loading of ca. 10 wt.% but the different N contents of supports from 0 to 12.0 at.%.

Reaction condition: 350 °C, 0.10 MPa, H_2/CO=1, gas hourly space velocity (GHSV) =12,000 mL h^{-1} g^{-1}.

With increasing N content from 0 to 12.0 at.%, the average sizes of Fe_3O_4 nanoparticles for the fresh catalysts decrease monotonously from 7.4 to 4.3 nm, accompanied by the narrowing of size distributions (a-e). The catalysts show a generally increasing tendency in sintering resistance (e, e'), since increasing N content favors a low partial pressure of the iron carbonyl intermediates ($p_{Fe(CO)_x}$) (see Fig. 1 c,d in the main text) by suppressing the formation of iron carbonyls.

The average size of nanoparticles on high-N-content hNCNC-3 is 'far' less than the corresponding one on hCNC (Fig. S3a,d), which should favor the formation of iron carbonyls for the former due to the higher surface energy. Hence, the inhibited carbonylation of the Fe_xC_y nanoparticles on N-containing supports is originated from the electronic effect due to N-doping rather than the geometric change.

From the morphological difference, the carbon deposition is arrowed in (a'-c'). We noticed that the carbon deposition became alleviated with increasing N content and even disappeared on the spent 10Fe/hNCNC-3 with the highest N content (12.0 at.%) (a'-d'), suggesting the favorable effect of nitrogen doping on the resistance to carbon deposition. The typical HRTEM image of carbon deposition is presented in Fig. S14.
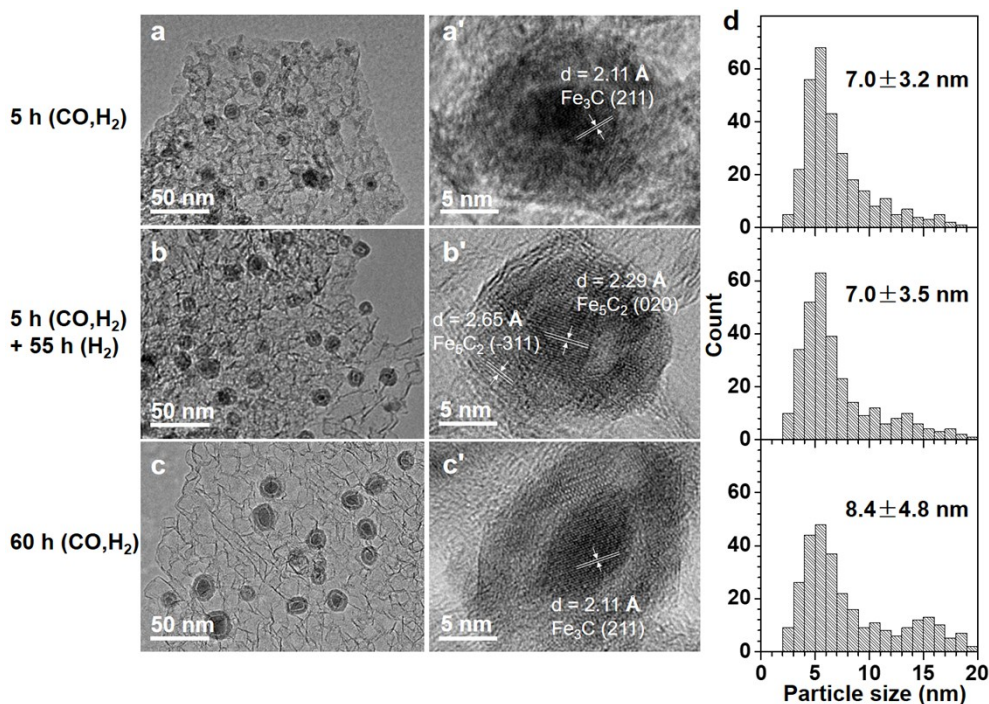
Fig. S4 TEM images (a-e, a'-e') and particle size distributions (f, f') of fresh catalysts (left) and spent catalysts after 60 h on stream in FTO (right). The catalysts have the different Fe loadings from 9.5 to 41.5 wt.% but the same high N content of 12.0 at.% for hNCNC-3 support.

Reaction condition: 350 °C, 0.10 MPa, $H_2/CO=1$, GHSV = 12,000 mL h^{-1} g^{-1}.

The average sizes of Fe_3O_4 nanoparticles for the fresh catalysts increase from 4.3 to 7.0 nm with increasing Fe loadings from 9.5 to 41.5 wt.% (a-e).

Notably, the catalyst of 9.5 wt.% Fe loading with the smallest average particle size presents the weaker sintering resistance than the others with Fe loading in the range of 20.1-41.5 wt.%, and more core-shell particles appear after reaction (a, a'). According to the iron carbonyl-mediated growth mechanism, the smaller size would generate the higher $P_{Fe(CO)_x}$ due to the higher surface energy, which is unfavorable for sintering resistance but favorable for the formation of core-shell particles. In general, in the precondition of well dispersion, increasing the average particle size makes the better performance of sintering resistance, and the less core-shell particles (a-d, a'-d').

Fig. S5 (HR)TEM images and particle size distributions of the 10Fe/hNCNC-3 catalyst. (a, a') After 5 h on stream. (b, b') After 5 h on stream followed by 55 h H_2 heat-treatment. (c, c') After 60 h on-stream. (d) Corresponding particle size histograms.
Reaction condition: 350 °C, 0.10 MPa, $H_2/CO=1$ or pure H_2, GHSV=12,000 mL h^{-1} g^{-1}.

The morphology and size distribution of Fe_xC_y nanoparticles in (a, b) are similar with each other, much different from the case in (c). The result indicates only a slight change in the H_2 heat-treatment process (b) but an obvious change in FTO process (c), which means a vital role of CO in the sintering of Fe_xC_y nanoparticles.

Note:

In the presence of CO, the chemical potential of carbon (μ_C) is high enough and the iron carbide phase is maintained (Fig. S5a'c').[10] Actually, the iron carbide phase is the well-known product in Fischer-Tropsch synthesis (also see Fig. 3 and Fig. S20). When the Fe_xC_y particles were treated in H_2 at 350 °C for 55 hours (without the presence of CO) (Fig. S5b,b'), the μ_C is extreme low, which favors the decomposition of Fe_xC_y particles into metallic iron. However, our HRTEM observations indicate the Fe_xC_y phase is still kept there (Fig. S5b'). Even though there was a slight decomposition of Fe_xC_y into metallic iron, the particle size should change little owing to its nature of interstitial compound. These results indicate the sintering of Fe_xC_y nanoparticles in this study is associated with the existing CO.

The HRTEM images of the shell present the well-oriented fringes for the Fe_xC_y phase (Fig. 3f, Fig. S5b'), which is different from the irregular fringes of the deposited carbon (Fig. S19b). Thus, the shell is made of polycrystalline Fe_xC_y rather than carbon.
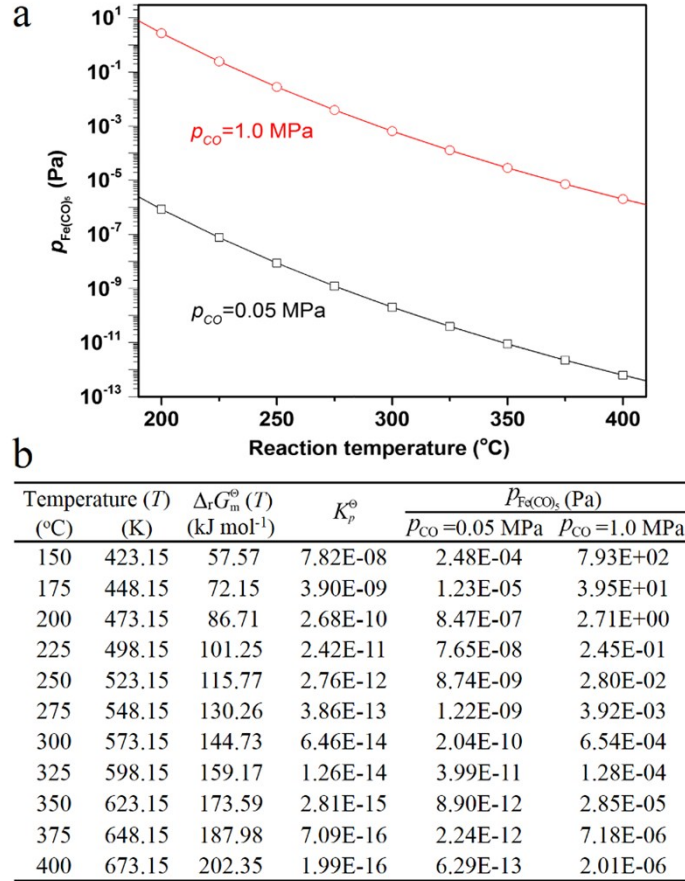
Fig. S6 Calculated equilibrium partial pressure of gaseous iron pentacarbonyl ($p_{Fe(CO)_5}$) under the designated reaction condition. (a) Plot of $p_{Fe(CO)_5}$ versus reaction temperature. (b) Detailed calculation data.

The plot (a) shows $p_{Fe(CO)_5}$ (Pa) on the y-axis (from 10^{-13} to 10^{1}) versus Reaction temperature (°C) on the x-axis (200 to 400), with two curves: p_{CO}=1.0 MPa and p_{CO}=0.05 MPa.

Table (b):

Temperature (T) (°C)	(K)	$\Delta_r G_m^\ominus(T)$ (kJ mol^{-1})	$K_p^\ominus$	$p_{Fe(CO)_5}$ (Pa) p_{CO}=0.05 MPa	p_{CO}=1.0 MPa
150	423.15	57.57	7.82E-08	2.48E-04	7.93E+02
175	448.15	72.15	3.90E-09	1.23E-05	3.95E+01
200	473.15	86.71	2.68E-10	8.47E-07	2.71E+00
225	498.15	101.25	2.42E-11	7.65E-08	2.45E-01
250	523.15	115.77	2.76E-12	8.74E-09	2.80E-02
275	548.15	130.26	3.86E-13	1.22E-09	3.92E-03
300	573.15	144.73	6.46E-14	2.04E-10	6.54E-04
325	598.15	159.17	1.26E-14	3.99E-11	1.28E-04
350	623.15	173.59	2.81E-15	8.90E-12	2.85E-05
375	648.15	187.98	7.09E-16	2.24E-12	7.18E-06
400	673.15	202.35	1.99E-16	6.29E-13	2.01E-06

Note: All gases are considered as ideal gas in calculation.

The standard molar Gibbs energies ($\Delta_r G^\ominus{}_m(T)$), equilibrium constant ($K^\ominus{}_p$) and equilibrium $p_{Fe(CO)_5}$ were calculated by taking an example of the formation of Fe(CO)$_5$ (g) via Fe$_3$C (s) and CO (g), as described below:

$$\frac{1}{3}Fe_3C(s) + 5CO(g) = Fe(CO)_5(g) + \frac{1}{3}C(s,\text{ graphite}) \tag{1}$$
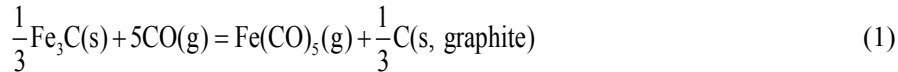
$$\Delta C_{p,m}^\ominus = C_{p,m}^\ominus(Fe(CO)_5) + \frac{1}{3}C_{p,m}^\ominus(C,\text{ graphite}) - \frac{1}{3}C_{p,m}^\ominus(Fe_3C) - 5C_{p,m}^\ominus(CO) \tag{2}$$

$$= \Delta a + \Delta bT + \Delta cT^2 + \Delta dT^3 + \Delta c'/T^2$$

$$\Delta_r H_m^\ominus(298.15\text{ K}) = \Delta_f H_m^\ominus(Fe(CO)_5) + \frac{1}{3}\Delta_f H_m^\ominus(C,\text{ graphite}) - \frac{1}{3}\Delta_f H_m^\ominus(Fe_3C) - 5\Delta_f H_m^\ominus(CO) \tag{3}$$

$$= -189.62\text{ kJ mol}^{-1}$$

$$\Delta_r H_m^\ominus(T) = \Delta_r H_m^\ominus(298.15\text{ K}) + \int_{298.15}^{T_2} \Delta C_{p,m}^\ominus dT \tag{4}$$

$$= \Delta_r H_m^\ominus(298.15\text{ K}) + \Delta aT + \frac{1}{2}\Delta bT^2 + \frac{1}{3}\Delta cT^3 + \frac{1}{4}\Delta dT^4 - \Delta c'/T + C$$

where $C = -(\Delta aT + \frac{1}{2}\Delta bT^2 + \frac{1}{3}\Delta cT^3 + \frac{1}{4}\Delta dT^4 - \Delta c'/T)\big|_{T=298.15} = 6.3361\text{ kJ mol}^{-1}$

$$\Delta_r G_m^\ominus(298.15\text{ K}) = \Delta_f G_m^\ominus(Fe(CO)_5) + \frac{1}{3}\Delta_f G_m^\ominus(C,\text{ graphite}) - \frac{1}{3}\Delta_f G_m^\ominus(Fe_3C) - 5\Delta_f G_m^\ominus(CO) \tag{5}$$

$$= -15.467\text{ kJ mol}^{-1}$$

9

According to Gibbs-Helmholtz formula：

$$d\left(\frac{\Delta_r G_m^{\Theta}(T)}{T}\right) = -\frac{\Delta_r H_m^{\Theta}(T)dT}{T^2}$$

(6)

$$= -\frac{(\Delta_r H_m^{\Theta}(298.15\ \mathrm{K}) + \Delta aT + \frac{1}{2}\Delta bT^2 + \frac{1}{3}\Delta cT^3 + \frac{1}{4}\Delta dT^4 - \Delta c'/T + C)dT}{T^2}$$

$$\frac{\Delta_r G_m^{\Theta}(T)}{T} = \frac{\Delta_r H_m^{\Theta}(298.15\ \mathrm{K})}{T} - \Delta a \ln T - \frac{1}{2}\Delta bT - \frac{1}{6}\Delta cT^2 - \frac{1}{12}\Delta dT^3 - \frac{\Delta c'}{2T^2} + \frac{C}{T} + I$$

(7)

$$\Delta_r G_m^{\Theta}(T) = \Delta_r H_m^{\Theta}(298.15\ \mathrm{K}) + C - \Delta aT \ln T - \frac{1}{2}\Delta bT^2 - \frac{1}{6}\Delta cT^3 - \frac{1}{12}\Delta dT^4 - \frac{\Delta c'}{2T} + IT$$

(8)

where

$$I = \left(\frac{\Delta_r G_m^{\Theta}(T) - \Delta_r H_m^{\Theta}(298.15\ \mathrm{K}) - C}{T} + \Delta a \ln T + \frac{1}{2}\Delta bT + \frac{1}{6}\Delta cT^2 + \frac{1}{12}\Delta dT^3 + \frac{\Delta c'}{2T^2}\right)\Big|_{T=298.15\ \mathrm{K}}$$
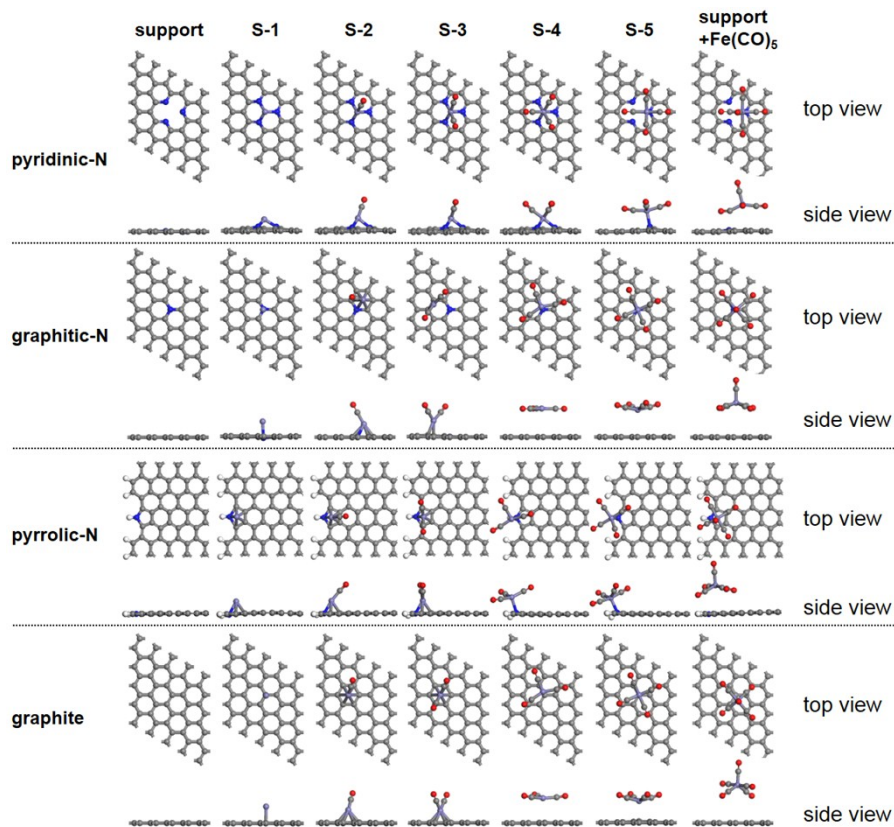
$$= 231.98\ \mathrm{J \cdot K^{-1} \cdot mol^{-1}}$$

$$Q \quad \Delta_r G_m^{\Theta}(T) = -RT \ln K_p^{\Theta}$$

(9)

$$\therefore\ K_p^{\Theta} = e^{\frac{-\Delta_r G_m^{\Theta}(T)}{RT}} = \frac{p_{Fe(CO)_5}/p^{\Theta}}{\left(p_{CO}/p^{\Theta}\right)^5} = \frac{p_{Fe(CO)_5}(p^{\Theta})^4}{\left(p_{CO}\right)^5}$$

(10)

$$\therefore\ p_{Fe(CO)_5} = K_p^{\Theta}\frac{(p_{CO})^5}{(p^{\Theta})^4}$$

(11)

$K\Theta\ p$ and $p_{Fe(CO)_5}$ were calculated by equation (10) and equation (11). p^{Θ} is the standard pressure, and the other thermodynamic parameters used in the calculations are presented in Table S3.

Fig. S7 The optimized configurations for the iron carbonylation processes on different supports. C: gray. N: blue. O: red. Fe: purple. H: white.

Note: The corresponding energy diagrams are presented in Fig. 1d in the main text and Fig. S8.

It is learnt that the detachment of the iron carbonyl species on pyridinic-N- and pyrrolic-N-doped support is more difficult than that on pristine graphite and graphitic-N-doped support.
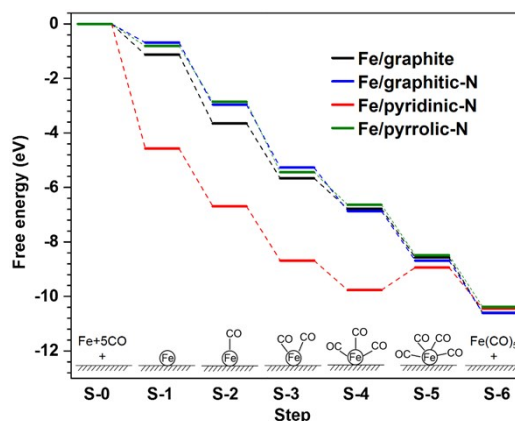
Fig. S8 The whole free energy diagrams for the formation of $Fe(CO)_5$ from a single Fe atom on the pristine and N-doped graphitic plane. The free energy of an isolated Fe atom + 5CO + support is selected as the referenced zero point. The optimized configurations are presented in Fig. S7.

The adsorption of a Fe atom (S-0 → S-1) on the pyridinic N-doped graphite plane releases more energy than that on the pristine graphite and the graphitic N- or pyrrolic N-doped graphite plane, suggesting the strong bind between Fe atom and pyridinic N.

The subsequent carbonylation of single Fe atom involves the spontaneous multistep reactions with large free-energy drops on all the sites except for the pyridinic-N (Figure S8). This means the absorbed iron sub-carbonyl species would quickly react with CO to produce gaseous iron (sub)carbonyls, with little chance for diffusion on the supports. For the pyridinic-N site, even the sub-carbonyls could migrate over the support to other sites, it will soon turn into gaseous $Fe(CO)_5$. Therefore, the migration of sub-carbonyls over the support should be a minor factor, in accordance with the strong correlation between the particle growth and the amount of gaseous $Fe(CO)_x$ species detected by in situ mass spectrometry (Fig. 1, 2 and Fig. S12).
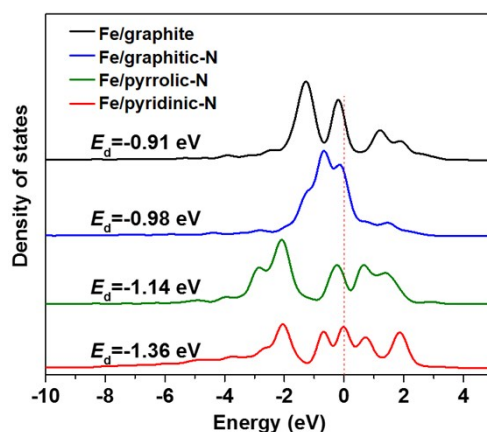
Fig. S9 The projected d-band states of Fe atom loaded on the pristine and nitrogen-doped graphitic plane. E_d is the projected d-band center. The Fermi levels are set to 0 eV as denoted by the dashed red line. The optimized configurations are presented in Fig. S7.
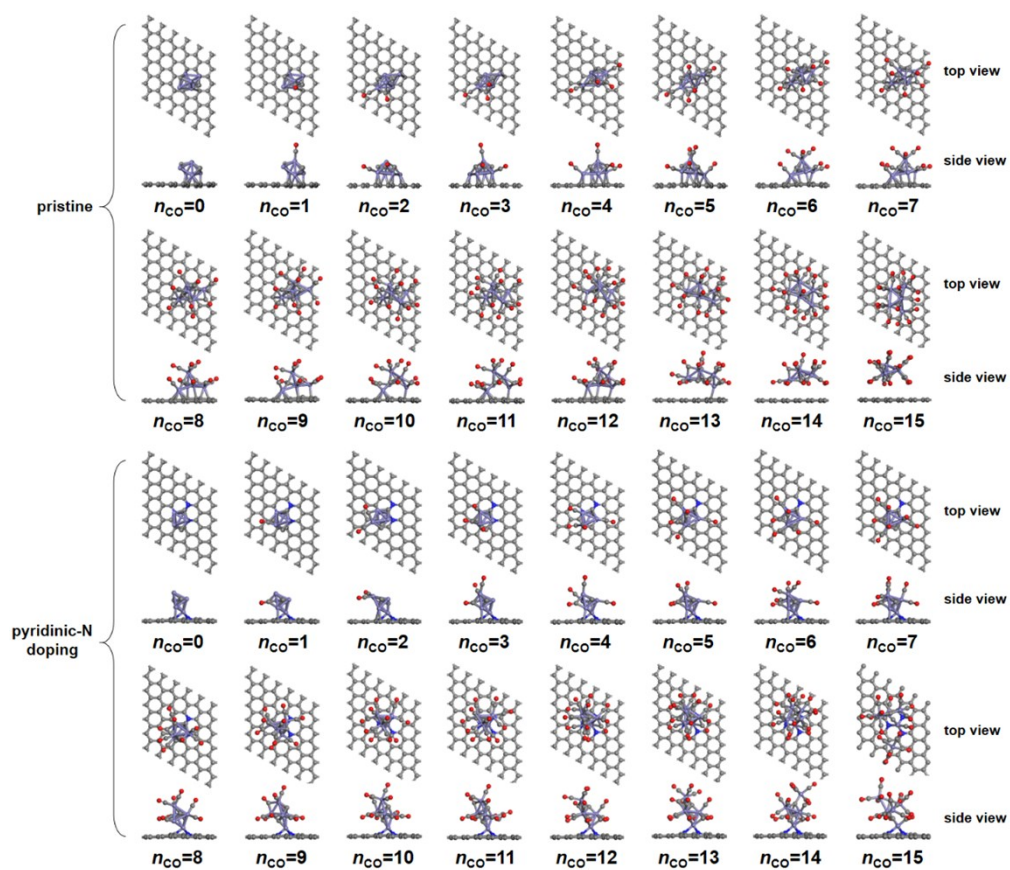
Fig. S10 The optimized configurations for the carbonylation process of an Fe_5C_2 cluster supported on pristine and pyridinic N-doped graphite plane, respectively. C: gray. N: blue. O: red. Fe: purple.

Note: The corresponding energy diagrams are presented in Fig. S11.
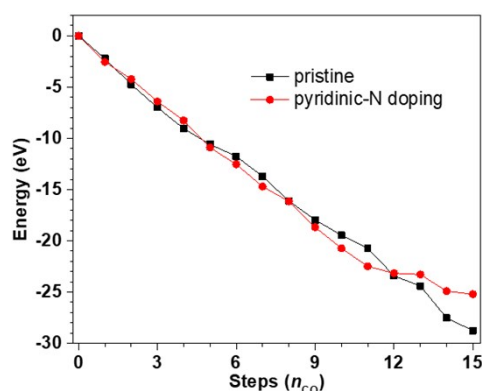
Fig. S11 Energy diagrams for the carbonylation on the Fe_5C_2 cluster supported on pristine and nitrogen-doped graphitic plane, respectively.

Note : The sum energy of the Fe_5C_2 cluster, 15CO and support is selected as the referenced zero point. The optimized configurations are presented in Fig. S10.

Fifteen carbonyls were added one by one to the Fe_5C_2 cluster models and the geometry optimization was performed for each step (Fig. S10). Both energy diagrams tangle together at the low coverage stage ($n_{CO} \leqslant 9$), and separate when approaching the saturation (Fig. S11). On the pristine support, the diagram drops linearly and the cluster detaches from the support when $n_{CO} \geq 14$. On the N-doped support, the diagram has an inflection at $n_{CO}=11$, thereafter the carbonylation process becomes less exothermic. The cluster keeps attached on the support even at $n_{CO}=15$. These results further support our experimental observations that the N-doping into carbon support could suppress the carbonylation of the active phase.

The theoretical study with the simple models of single iron atom or Fe_5C_2 cluster on a carbon sheet (Fig. S7-S11) demonstrates the suppression effect of N-doping on the formation of iron carbonyls. It's really hard to simulate the 'real' case with the large particle model (thousands of atoms) due to the huge and complicated calculations. Anyhow, the simulation results in the two simple models are helpful to understand the N-doping effect for suppressing the formation of iron carbonyls.
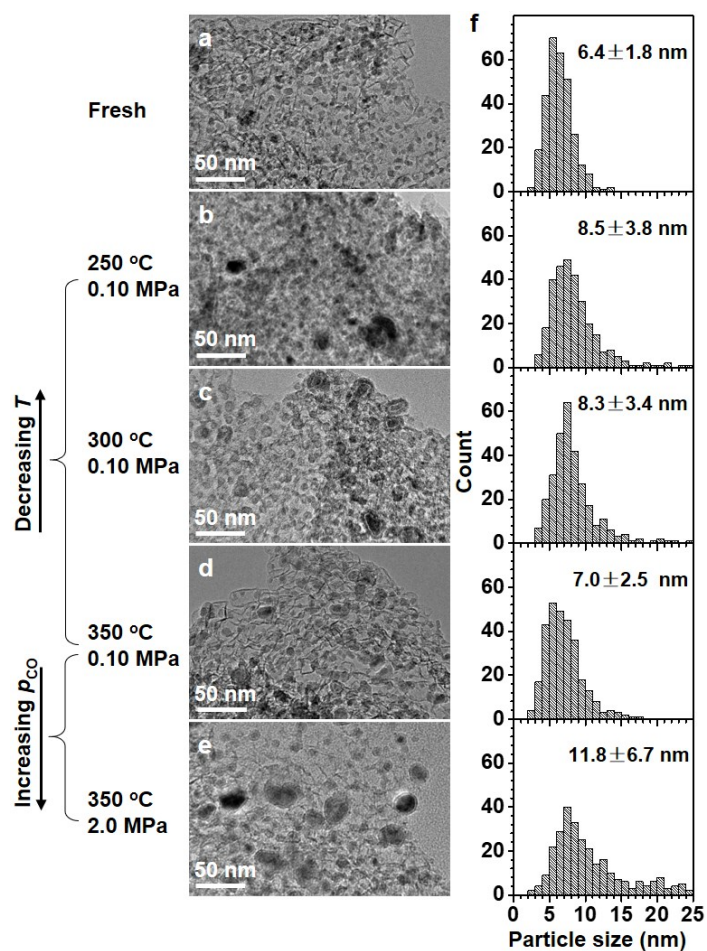
Fig. S12 TEM examination on the effect of reaction temperature/pressure on 35Fe/hNCNC-3 sintering. (a) Fresh catalyst. (b-e) Spent catalysts with the marked T and P_{CO}. (f) Corresponding particle size distributions.

Reaction condition: $H_2/CO=1$, GHSV=12,000 mL h^{-1} g^{-1}, TOS=60 h.

The Fe$_x$C$_y$ nanoparticles get more sintered with decreasing T or increasing p_{co}.

Decreasing T (b-d) or increasing P_{CO} (d,e) increases $P_{Fe(CO)_x}$ (see Fig. 1c in the main text), which leads to the more serious catalyst sintering as expected according to the iron carbonyl-mediated growth mechanism.

15
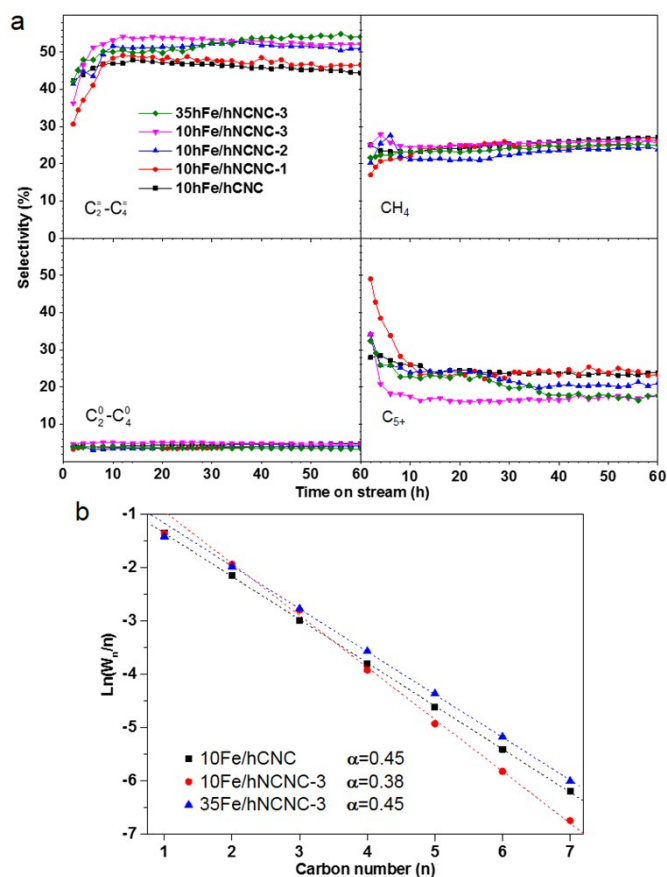
Fig. S13 Product selectivities (a) and corresponding Anderson-Schulz-Flory (ASF) plots (b) of different catalysts.

Reaction condition: 350 °C, 0.10 MPa, CO/H_2=1, GHSV=12,000 mL h^{-1} g^{-1}, TOS=60 h.

After ca. 10 h activation, the selectivities of the catalysts kept relatively steady. According to the ASF model[11], the maximum selectivity toward C= 2-C= 4 is achieved with the chain-growth probability (α value) of 0.4~0.5. For 10Fe/hCNC, 10Fe/hNCNC-3 and 35Fe/hNCNC-3 catalysts, α values are estimated to be 0.45, 0.38 and 0.45, respectively, within or very close to the optimal range of α value.

Fresh   **Spent**

10Fe/hCNC   a   50 nm

d   7.4±3.0 nm   d'   22.1±8.9 nm   a'   50 nm

10Fe/hNCNC-3   b   50 nm

4.3±1.5 nm   10.0±5.6 nm   b'   50 nm

35Fe/hNCNC-3   c   50 nm

6.4±1.8 nm   10.7±6.6 nm   c'   50 nm
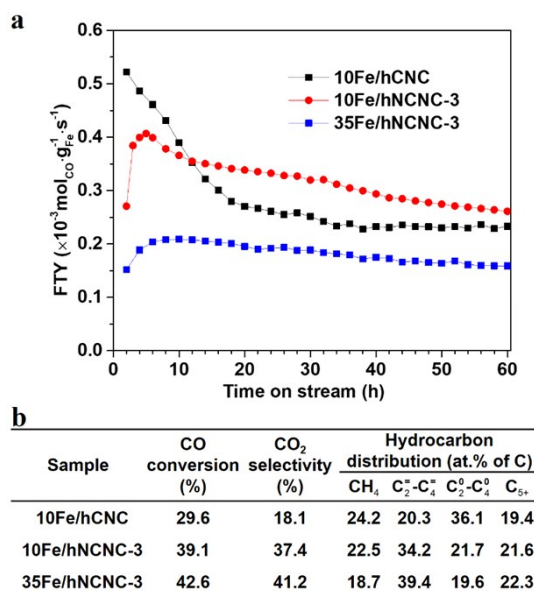
Count
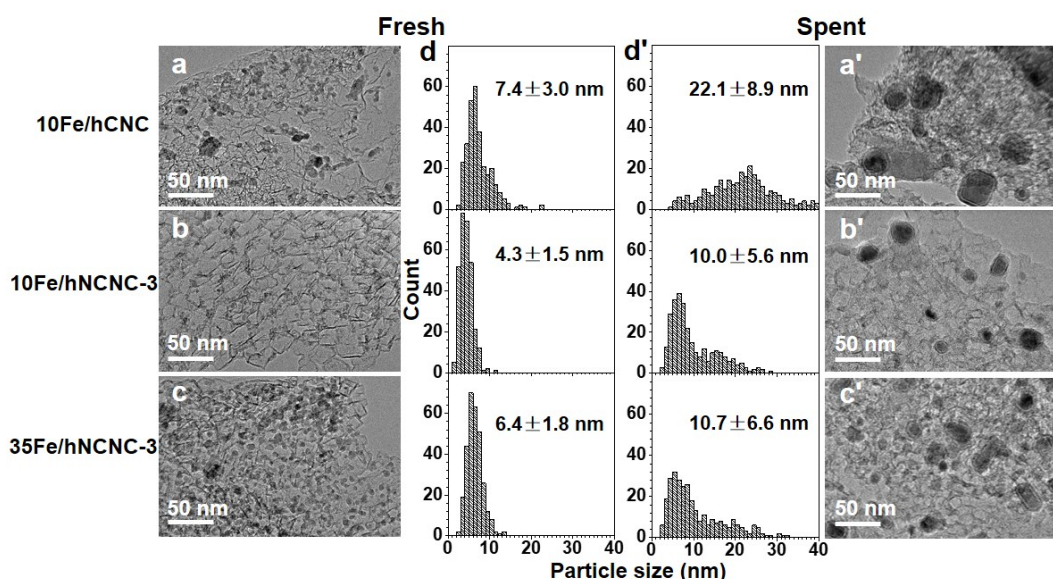
Particle size (nm)

Fig. S14 TEM images (a-c, a'-c') and corresponding particle size distributions (d, d') of the fresh catalysts (left) and the spent catalysts after 60 h on stream at the pressure of 1.0 MPa (right).
Reaction condition: 350 °C, $H_2/CO=1$. GHSV is 12,000 mL h^{-1} g^{-1} for the 10Fe/hCNC and 10Fe/hNCNC-3 catalysts, and 24,000 mL h^{-1} g^{-1} for the 35Fe/hNCNC-3 catalyst.
Note: The corresponding FTO performance and descriptions are presented in Fig. S15.

The change behavior is similar to the case at the low pressure (0.10 MPa) (see Fig. S3a,a',e,e' for 10Fe/hCNC, and Fig. S4a,a',d,d',f,f' for 10Fe/hNCNC-3 and 35Fe/hNCNC-3), which also demonstrates the stabilizing effect of the N-doped carbon support on the Fe-based active phase size.

a

FTY ($\times 10^{-3}$ mol$_{CO}$·g$_{Fe}^{-1}$·s^{-1})

- ■ 10Fe/hCNC
- ● 10Fe/hNCNC-3
- ■ 35Fe/hNCNC-3

Time on stream (h)

b

Sample	CO conversion (%)	CO$_2$ selectivity (%)	Hydrocarbon distribution (at.% of C)			
			CH$_4$	C$_2^=$-C$_4^=$	C$_2^0$-C$_4^0$	C$_{5+}$
10Fe/hCNC	29.6	18.1	24.2	20.3	36.1	19.4
10Fe/hNCNC-3	39.1	37.4	22.5	34.2	21.7	21.6
35Fe/hNCNC-3	42.6	41.2	18.7	39.4	19.6	22.3

Fig. S15 FTO performance of the catalysts at the pressure of 1.0 MPa. (a) Iron time yield (FTY), expressing the moles of the converted CO per gram of Fe per second. (b) The conversion and selectivity at TOS=60 h. The reaction condition is presented in Fig. S14.

Similar to the case at the low pressure (0.10 MPa), the results at the high pressure (1.0 MPa) also demonstrate the stabilizing effect of the N-doped carbon support on the Fe-based active phase size (Fig. S14). Compared to the data at the low pressure (Table 1 in the main text), the selectivity of lower olefins decreased while that of lower alkanes increased. Anyway, the improvement of the N-doping to FTO selectivity is still obvious.
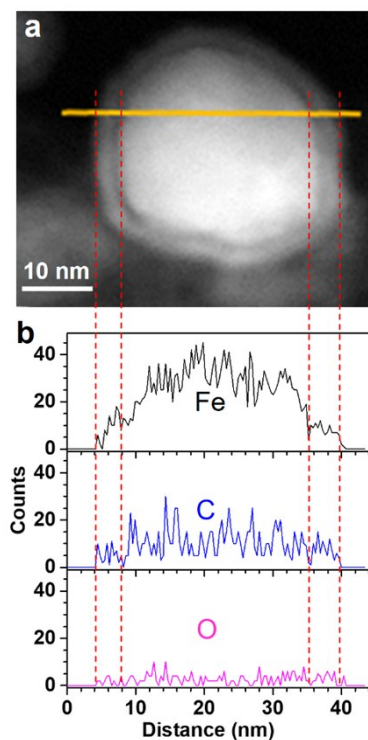
17
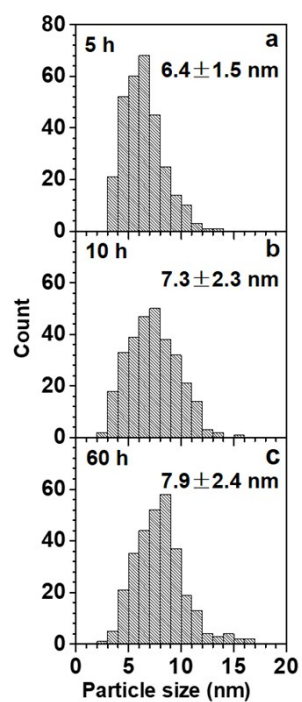
Fig. S16 Core size distribution of the core-shell nanoparticles of spent 10Fe/hNCNC-3 after 5, 10 and 60 h on stream in FTO, derived from Fig. 3b-d.

**Reaction condition:** 0.10 MPa, 350 $^{\circ}$C, GHSV=12,000 mL h^{-1} g^{-1}.

The average core size increases from 6.4 to 7.3 and 7.9 nm with increasing the reaction time from 5 to 10, and 60 h, respectively.

Fig. S17 Composition analysis of the core-shell particles in the spent catalyst. (a) Scanning TEM image. (b) EDS profiles of Fe, C, and O corresponding to the yellow line in (a).

The EDS result indicates that both the core and shell present the signals of carbon and iron. In contrast, the signal of oxygen is very weak and featureless, which is attributed to the adsorbed oxygen and/or surface-oxidized iron species due to the exposure in air. This result, together with the HRTEM observation in Fig. 3f of the main text, confirms that the shell layer is mainly composed of the iron carbides rather than the iron oxides or carbon deposition.
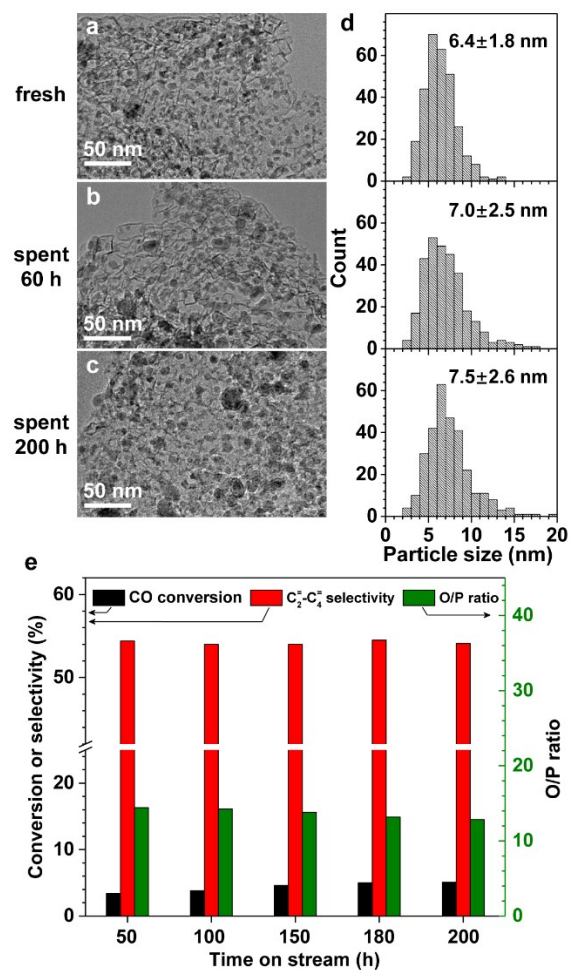
Fig. S18 Evolutions of morphology and particle size distribution of the 35Fe/hNCNC-3 catalyst. (a-c) TEM images of fresh and spent catalyst after 60 h and 200 h. (d) Corresponding particle size distribution from 300 nanoparticles. (e) FTO performance of 35Fe/hNCNC-3 catalyst for TOS of 50, 100, 150, 180 and 200 h, respectively.

Reaction condition: 350 °C, 0.10 MPa, CO/H_2=1, GHSV=12,000 mL h^{-1} g^{-1}.

Even after 200 h on-stream in FTO, the average particle size of Fe nanoparticles only slightly increases by ~1.0 nm, meanwhile without observable carbon deposition, demonstrating the outstanding stability. A slow increase of the CO conversion with time should originate from the optimization of the particle sizes and/or continued iron carbide formation.[12,13]
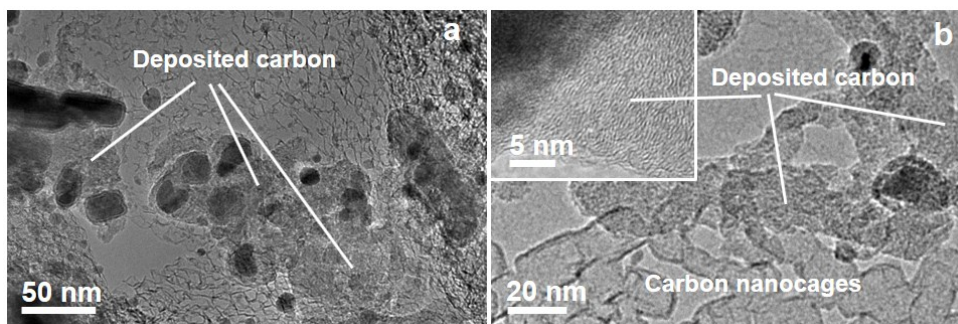
Fig. S19 TEM images of the spent 10Fe/hCNC catalyst after 60 h on stream (a, b). Inset in (b) is the typical HRTEM image of deposited carbon.
Reaction condition: 350 ^{o}C, 0.10 MPa, H_2/CO=1, GHSV=12,000 mL h^{-1} g^{-1}.

According to the morphological difference, the typical carbon deposition is marked here which is much different from the cage-shaped hCNC or hNCNC in Fig. S1 and S3.

IS (mm·s⁻¹)	QS (mm·s⁻¹)	H (T)	Γ (mm·s⁻¹)	Phase ascription	A (%)
0.06	0.48		0.65	Fe_xC	19.2
0.07		21.0	0.58	$Fe_5C_2(A)$	13.9
0.26		11.0	0.62	$Fe_5C_2(B)$	12.0
1.01	0.93		0.90	Fe^{2+}	38.4
1.09			0.79	Fe^{2+}	16.6
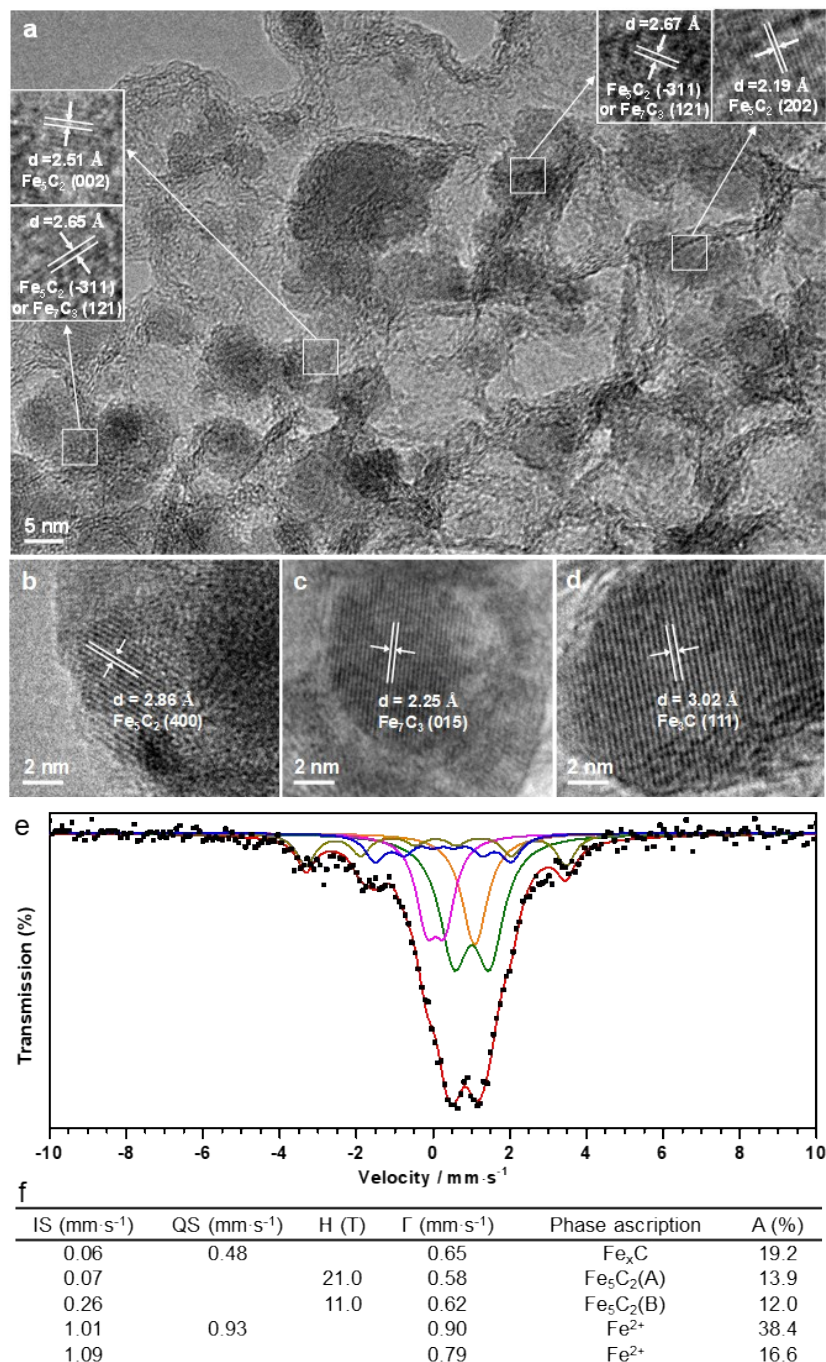
Fig. S20 HRTEM and Mössbauer characterizations on the spent 35Fe/hNCNC-3. (a-d) HRTEM images. (e,f) Mössbauer spectrum and corresponding fitting parameters.
IS_isomer shift (relative to α-Fe); QS_quadrupole splitting; H_hyperfine magnetic field; Γ_the full width at half-maximum; A_relative spectral area.
Reaction condition: 350 °C, 0.10 MPa, CO/H_2=1, GHSV=12,000 mL h⁻¹ g⁻¹, TOS=60 h.

In (a-d), the lattice spacings of the nanoparticles can be assigned to χ-Fe_5C_2, Fe_7C_3 and θ-Fe_3C (JCPDS No.: 089-8968, 075-1499 and 089-7271). Iron carbide species were detected in Mössbauer spectrum with the total content of 45.1 mol%, and the remaining Fe species presented in Fe^{2+} (e,f).[14]

It should be mentioned that, due to the superparamagnetic relaxation, the room-temperature Mössbauer spectrum presents the collapsed one which could qualitatively rather than quantitatively

examine the Fe-containing phases. Hence the relative content (A%) in Fig. S20f is just for reference.

Table S1. BET specific surface areas and element contents of hNCNC and hCNC.

Samples	S_{BET} [a] (m^2 g^{-1})	Mesopore surface area (m^2 g^{-1})	Micropore volume (cm^{-3}g^{-1})	Content (at.%) [b]						
				N					C	O
				total	pyridinic	pyrrolic	graphitic	N-oxide		
hCNC	2073	1696	0.80	-	-	-	-	-	97.3	2.7
hNCNC-1	1894	1455	0.67	3.0	0.7 (24.4)[c]	0.1 (2.3)	2.0 (66.5)	0.2 (6.8)	94.5	2.5
hNCNC-2	2186	1764	0.87	8.1	2.1 (26.3)	0.7 (9.1)	4.8 (58.9)	0.5 (5.6)	89.5	2.4
hNCNC-3	1805	1439	0.75	12.0	3.9 (32.2)	2.4 (19.8)	4.3 (35.7)	1.5 (12.3)	84.2	3.8

Note: [a] S_{BET}, mesopore surface area and micropore volume were calculated based on the adsorption data in Fig. S1g, and the corresponding pore size distributions are presented in Fig. S1h. [b] The element contents were detected by XPS (Fig. S1i). [c] The data in parentheses refer to the relative percentage of nitrogen species.

Table S2 Properties and basic parameters of the catalysts.

Sample	Fe loading[a] (wt.%)	FTY[b] (×10^{-6} mol$_{CO}$·g-1 Fe·s^{-1})	Average particle size (nm)[c]		Size for the particle in different phases (nm)[d]	
			Fresh	Reduced	FeO	Fe
10Fe/hCNC	9.0	13.3	7.4	6.9	7.0	5.8
10Fe/hNCNC-1	12.4	13.1	6.9	6.6	6.5	5.4
10Fe/hNCNC-2	10.1	13.2	6.4	6.0	6.0	5.0
10Fe/hNCNC-3	9.5	11.2	4.3	4.1	4.1	3.3
20Fe/hNCNC-3	20.1	7.4	5.7	5.4	5.4	4.5
30Fe/hNCNC-3	31.4	6.3	6.1	5.8	5.7	4.8
35Fe/hNCNC-3	36.8	6.7	6.4	6.1	6.0	5.0
40Fe/hNCNC-3	41.5	5.5	7.0	6.8	6.6	5.5

[a] Fe loading is measured by TG. [b] FTY is calculated based on the data in Table 1 in main text. [c] The average particle sizes were measured from TEM images. Reduction condition: 350 °C in H$_2$ flow for 2 h. [d] The particle sizes are calculated by constructing the corresponding nanoparticle models of same Fe numbers with Materials Studio Visualizer.

Generally, increasing the N-doping or Fe loading leads to the decrease of FTY, in consistent with the literature report.[15]

The H$_2$ reduction only slightly reduced the particle sizes of the catalysts. Hence, we compared the change of the particle sizes of the fresh and spent catalysts in the manuscript for clarity.

Table S3. Standard enthalpies of formation ($\Delta_f H^\ominus$), Gibbs energies of formation ($\Delta_f G^\ominus$), standard entropies ($S^\ominus$), and heat capacities ($C_{p,\,m}$) of iron carbide, carbon monoxide, iron pentacarbonyl, graphite and carbon dioxide.

Substance	$\Delta_f H^\ominus$ (kJ mol^{-1})	$\Delta_f G^\ominus$ (kJ mol^{-1})	$S^\ominus$ (J mol^{-1} K^{-1})	$C_{p,\,m}$				$C_{p,\,m} = a + bT + cT^2 + dT^3 + c'/T^2$				
				400 K	600 K	800 K	1000 K	a (J mol^{-1} K^{-1})	b (10^{-3} J mol^{-1} K^{-2})	c (10^{-6} J mol^{-1} K^{-3})	d (10^{-9} J mol^{-1} K^{-4})	c' (10^6 J mol^{-1} K)
Fe$_3$C(s)	25.11	20.09	104.65	115.70	114.78	117.30	119.80	141.57	-121.90	171.60	-71.508	-
CO(g)	-110.59	-137.76	197.99	-	-	-	-	25.567	6.096	4.055	-2.671	0.1310
Fe(CO)$_5$(g)	-734.2	-697.57	445.37	189.0	209.8	223.1	232.2	111.70	269.25	-217.50	68.750	-
C(s, graphite)	0	0	5.70	12.0	16.6	19.7	21.7	-3.30	50.420	-33.750	8.333	-
CO$_2$(g)	-393.68	394.56	213.77	-	-	-	-	24.997	55.187	-33.691	7.948	-0.1366

Note: All data of $\Delta_f H^\ominus$, $\Delta_f G^\ominus$ and $S^\ominus$ come from Lange's Handbook of Chemistry (13th Edition), by multiplying 4.18585 to convert the unit from calorie (cal.) to joule (J). The $C_{p,\,m}$ of Fe$_3$C(s), Fe(CO)$_5$(g) and C(s, graphite) at the four temperatures come from Lange's Handbook of Chemistry (15th Edition), which are fitted by the formula of $C_{p,\,m} = a + bT + cT^2 + dT^3$. $C_{p,\,m}$ of CO and CO$_2$ come from NIST Chemistry WebBook, SRD (http://webbook.nist.gov/chemistry/form-ser/).

References

(1) J. Zhao, H. W. Lai, Z. Y. Lyu, Y. F. Jiang, K. Xie, X. Z. Wang, Q. Wu, L. J. Yang, Z. Jin, Y. W. Ma, J. Liu and Z. Hu, *Adv. Mater.*, 2015, **27**, 3541–3545.

(2) B. Delley, *J. Chem. Phys.*, 1990, **92**, 508–517.

(3) B. Delley, *J. Chem. Phys.*, 2000, **113**, 7756–7764.

(4) J. P. Perdew, K. Burke and M. Ernzerhof, *Phys. Rev. Lett.*, 1996, **77**, 3865–3868.

(5) P. Hohenberg and W. Kohn, *Phys. Rev.*, 1964, **136**, B864.

(6) W. Kohn and L. J. Sham, *Phys. Rev.*, 1965, **140**, A1133–A1138.

(7) M. C. Payne, M. P. Teter, D. C. Allan, T. A. Arias and J. D. Joannopoulos, *Rev. Mod. Phys.*, 1992, **64**, 1045–1097.

(8) B. G. Pfrommer, M. Côté, S. G. Louie and M. L. Cohen, *J. Comput. Phys.*, 1997, **131**, 233–240.

(9) C. K. Acharya and C. H. Turner, *Surf. Sci.*, 2008, **602**, 3595–3602.

(10) E. de Smit, F. Cinquini, A. M. Beale, O. V. Safonova, W. van Beek, P. Sautet and B. W. Weckhuysen, *J. Am. Chem. Soc.*, 2010, **132**, 14928–14941.

(11) H. M. Torres Galvis and K. P. de Jong, *ACS Catal.*, 2013, **3**, 2130–2149.

(12) K. Cheng, J. C. Kang, D. L. King, V. Subramanian, C. Zhou, Q. H. Zhang and Y. Wang, *Adv. Catal.*, 2016, **60**, 125–208.

(13) M. Oschatz, S. Krause, N. A. Krans, C. H. Mejía, S. Kaskelb and K. P. de Jong, *Chem. Commun.*, 2017, **53**, 10204–10207.

(14) J. X. Xie, H. M. Torres Galvis, A. C. J. Koeken, A. Kirilin, A. I. Dugulan, M. Ruitenbeek and K. P. de Jong, *ACS Catal.*, 2016, **6**, 4017–4024.

(15) G. G. Liu, Q. J. Chen, E. Oyunkhand, S. Y. Ding, N. Yamane, G. H. Yang, Y. Yoneyama and N. Tsubaki, *Carbon*, 2018, **130**, 304–314.